PROCEEDINGS B

rspb.royalsocietypublishing.org

Research

Cite this article: Bicknell RDC, Ledogar JA, Wroe S, Gutzler BC, Watson III WH, Paterson JR. 2018 Computational biomechanical analyses demonstrate similar shell-crushing abilities in modern and ancient arthropods. *Proc. R. Soc. B* **285**: 20181935. http://dx.doi.org/10.1098/rspb.2018.1935

Received: 28 August 2018
Accepted: 5 October 2018

Subject Category:
Morphology and biomechanics

Subject Areas:
evolution, biomechanics, palaeontology

Keywords:
Limulus polyphemus, *Sidneyia inexpectans*, finite-element analysis, durophagy, Cambrian, Euarthropoda

Author for correspondence:
Russell D. C. Bicknell
e-mail: rdcbicknell@gmail.com

Computational biomechanical analyses demonstrate similar shell-crushing abilities in modern and ancient arthropods

Russell D. C. Bicknell[1,2], Justin A. Ledogar[1,2,3], Stephen Wroe[1,2], Benjamin C. Gutzler[4], Winsor H. Watson III[4] and John R. Paterson[1]

[1]Palaeoscience Research Centre, School of Environmental and Rural Science, and [2]Function, Evolution and Anatomy Research Lab, School of Environmental and Rural Science, University of New England, Armidale, New South Wales 2351, Australia
[3]Department of Evolutionary Biology, Duke University, Durham, NC 27708, USA
[4]Department of Biological Sciences and School of Marine Science and Ocean Engineering, University of New Hampshire, Durham, NH 03824, USA

RDCB, 0000-0001-8541-9035; SW, 0000-0002-6365-5915

The biology of the American horseshoe crab, *Limulus polyphemus*, is well documented—including its dietary habits, particularly the ability to crush shell with gnathobasic walking appendages—but virtually nothing is known about the feeding biomechanics of this iconic arthropod. *Limulus polyphemus* is also considered the archetypal functional analogue of various extinct groups with serial gnathobasic appendages, including eurypterids, trilobites and other early arthropods, especially *Sidneyia inexpectans* from the mid-Cambrian (508 Myr) Burgess Shale of Canada. Exceptionally preserved specimens of *S. inexpectans* show evidence suggestive of durophagous (shell-crushing) tendencies—including thick gnathobasic spine cuticle and shelly gut contents—but the masticatory capabilities of this fossil species have yet to be compared with modern durophagous arthropods. Here, we use advanced computational techniques, specifically a unique application of 3D finite-element analysis (FEA), to model the feeding mechanics of *L. polyphemus* and *S. inexpectans*: the first such analyses of a modern horseshoe crab and a fossil arthropod. Results show that mechanical performance of the feeding appendages in both arthropods is remarkably similar, suggesting that *S. inexpectans* had similar shell-crushing capabilities to *L. polyphemus*. This biomechanical solution to processing shelly food therefore has a history extending over 500 Myr, arising soon after the first shell-bearing animals. Arrival of durophagous predators during the early phase of animal evolution undoubtedly fuelled the Cambrian 'arms race' that involved a rapid increase in diversity, disparity and abundance of biomineralized prey species.

1. Introduction

Modern predatory arthropods use a range of morphological structures to acquire and consume food [1]. Some of the oldest fossil arthropods display masticatory spines called gnathobases: tooth-like projections located on the proximal margins of cephalic and trunk appendages [2–5]. Gnathobases are common in various (typically predatory) arthropod clades throughout the Phanerozoic [2–12]. However, only one extant group has gnathobases developed on a series of appendages: the xiphosurids, true horseshoe crabs [1]. Within Xiphosurida is the iconic American horseshoe crab, *Limulus polyphemus*: a species that shreds soft prey and crushes shell (durophagy) using gnathobases on coxal segments of cephalothoracic appendages II–VI [13–15]. Adduction of opposing coxae in the transverse plane optimizes *L. polyphemus* appendages for crushing and shredding [1,16].

THE ROYAL SOCIETY PUBLISHING

The *L. polyphemus* feeding apparatus is an ideal modern analogue for testing and quantifying ideas regarding feeding mechanics of extinct arthropods with gnathobase-bearing appendages, including eurypterids [6,17], trilobites [18] and disparate Cambrian taxa, such as the early Cambrian (*ca* 518 Ma) radiodontan *Amplectobelua symbrachiata* [3], and the mid-Cambrian (*ca* 508 Ma) euarthropod *Sidneyia inexpectans* [4,19,20]. *Sidneyia inexpectans* in particular, from the Burgess Shale of British Columbia, Canada [21], is often compared with *L. polyphemus*, due to their similar walking appendages [19,22–24]. Heavily sclerotized gnathobases on *S. inexpectans* appendages would have allowed it to crush shell, akin to *L. polyphemus* [4,19,22,24]. This is supported by the microstructural similarity of *L. polyphemus* and *S. inexpectans* gnathobases, and specimens of *S. inexpectans* with shelly gut contents [4,19,20,22]. However, just how effective *S. inexpectans* was at processing prey, particularly crushing shells, or how its mechanical performance might have compared with a modern analogue such as *L. polyphemus* [17], has never been tested. This is a central question regarding the feeding ecology of Cambrian arthropods. Addressing this question has important implications for understanding early animal evolution in the Cambrian, as the first durophages probably evolved at this time and helped escalate a major diversification of biomineralized prey species [20]. Here, we digitally reconstruct and simulate the feeding apparatus in *L. polyphemus* and *S. inexpectans*, and apply three-dimensional (3D) finite-element analysis to compare shapes of the two masticatory structures and test whether the shell-crushing tools of these two taxa, separated by 500 Myr, were functionally similar.

3D biomechanical modelling is a powerful tool that allows researchers to non-destructively predict mechanical performance in living and extinct animals. 3D FEA, specifically, can qualitatively and quantitatively predict how stresses and strains are distributed through biological features [25]. However, most FEA studies have considered vertebrate groups [26]. The limited arthropod FEA studies have mostly examined the performance of insect legs and wings [27–31], with rare studies showing the mechanical performance of mandibles and pincers [32–36]. The first 3D finite-element model (FEM) of a micro-computer tomography (micro-CT) scanned *L. polyphemus* coxa is presented to further develop arthropod-focused FEA research. Gnathobasic feeding is modelled and a strain contour map is produced. Distribution of von Mises microstrain and reaction force values at constrained gnathobases is calculated. A validation test involving comparison of bite reaction forces to FEM reaction forces using a live specimen is also presented.

Conducting FEA on extant groups allows strain patterns and magnitudes of modern analogues to be compared with extinct taxa [37–40]. FEA on extinct arthropods has never been conducted. Here we present the first application of 3D FEA to a well-known Cambrian gnathobase-bearing euarthropod: *Sidneyia inexpectans*. We conducted analyses using our three-dimensional reconstructions of the gnathobase-bearing segments of the walking appendages, the protopodite and coxa, of *S. inexpectans* and *L. polyphemus*, respectively. Here, we assume that *S. inexpectans* was one of the first Cambrian durophages and explore this assumption by qualitatively comparing the microstrain distributions and magnitudes of the *S. inexpectans* protopodite with the *L. polyphemus* coxa—the only appropriate modern analogue—and statistically analyse microstrain patterns of both taxa. Understanding the biomechanics of the *S. inexpectans* protopodite and its bearing on durophagous feeding allows us to explore questions about how this iconic Cambrian animal potentially impacted the benthic community of an early complex marine ecosystem. For example, was *S. inexpectans* only capable of crushing small, thin-shelled prey, as the gut contents would suggest?

2. Methods

(a) *Limulus polyphemus* model and validation

A female *L. polyphemus* specimen from the Marine Biological Laboratory at Woods Hole, USA was used for the FEM. The specimen was submerged in 1% iodine-ethanol solution for 13 days and washed in 100% ethanol for 2 days prior to scanning (see methods in [15,41,42]); staining increased muscle density. Muscles used in mastication were made easier to identify in the micro-CT scan and allowed muscle cross-sectional area (MCSA) data of adductor muscles to be gathered. These data are a proxy for the muscle forces that inform the feeding simulation described below. The specimen was scanned using computed tomography (CT) in the micro-CT scanner (GE-Phoenix V|tome|xs micro-CT scanner with 240 kV 'Direct' tube) at the University of New England, New South Wales. Data were captured using Datos acquisition software v. 2.2.1 (Phoenix, Wunstorf, Germany) and reconstruction software v. 2.2.1 RTM. The specimen was mounted on a rotating stage and imaged using optimized X-ray tube settings (150 kV, 200 µA, 200 ms integration time per projection). Projections (3600 in 360°) were captured using a 2000 × 2000 pixel 'virtual' (moving) detector array. Isotropic voxel side length was 92 µm. The GE constant rotation CT function was used to improve acquisition time and sample movement. Scan consisted of 1000 slices.

The scan was imported into Mimics v. 20 (Materialise, Leuven, Belgium). The posterior-most pair of walking legs (cephalothoracic appendage set V), dorsal cephalothoracic cuticle above the appendages, muscles used in mastication (discussed below) and endosternite (internal structure to which mastication muscles attach) were segmented out using the Mimics 'segmenting' tool. Cephalothoracic appendage set V was modelled because these appendages, coupled with the pushing legs (set VI), are the primary shell-crushing tools (as observed during the validation test). Notably, gnathobases on set V are also the most morphologically similar to *Sidneyia inexpectans* gnathobases [4]. Segmented exoskeletal components were converted to STL files in Mimics 20 and imported into Geomagic Studio (3D Systems, North Carolina, USA). Exoskeletal components were smoothed in Geomagic Studio. Smoothed STL files were exported from Geomagic Studio and a 3D PDF was generated using 3D Reviewer (Adobe Systems), following Bicknell *et al.* [15] and Lautenschlager *et al.* [43]. Distinct elements were assigned different colours (figure 1*c*). 3D PDF is presented as a supplementary file (figure S1 [70]).

Limulus polyphemus muscles involved in food processing are attached to epidermal cells on the inside of the exoskeleton. A digital dissection of muscles within the stained specimen was used to calculate MCSA values for the FEM, as muscle divisions are clearer in micro-CT scans than in gross dissections [16,42,44]. Furthermore, delicate muscles are often disturbed or destroyed during gross dissection [44]. Destruction of these muscles would have decreased muscle weights and therefore underestimated muscle force for the FEM. Muscles included in this study are those that adduct the coxae. Wyse & Dwyer ([16], p. 574) noted that muscles 25, 27–29 and 38–40 (their numbers) are all variably involved in adduction, but '38 [anterior], 38 [posterior], 39, and 40 … serve as the main adductors'. As such, only muscles 38 (anterior and posterior parts), 39 and 40 were segmented and used (figure 1*c*). MCSA values (mm^2) from CT scans are collected by reviewing the segmented muscles and measuring the muscle's thickest area, perpendicular to the

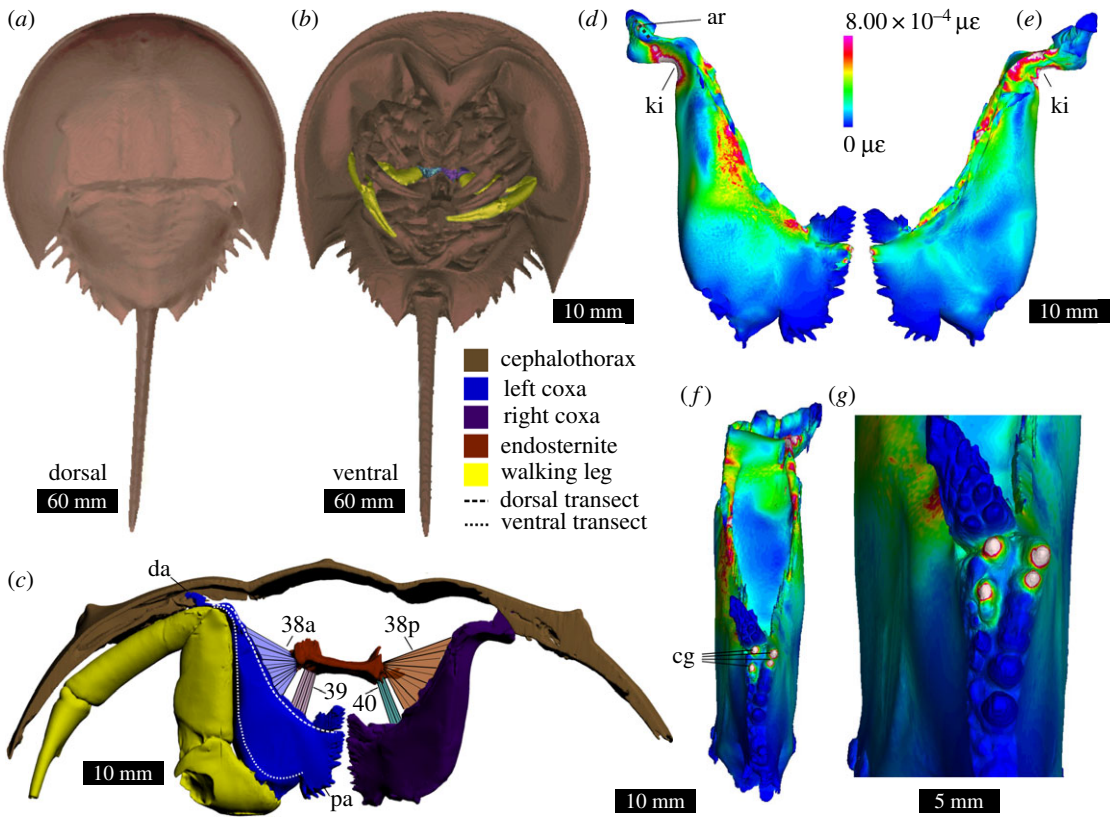

Figure 1. 3D reconstruction of *Limulus polyphemus* and von Misses (VM) microstrain maps. (*a*,*b*) 3D reconstruction of *L. polyphemus* specimen (Va.06) figured by Bicknell *et al*. [15], highlighting the position of the studied appendages (cephalothoracic appendage set V). Specimen is housed in the Natural History Museum of the University of New England (Armidale, New South Wales, Australia). (*a*) Va.06 in dorsal view. (*b*) Va.06 in ventral view. Colours correspond to coloured parts in (*c*). (*c*) Studied cephalothoracic section in anterior view. The 3D PDF is presented in figure S1 [70]. Muscles 38, 39 and 40 used in FEM are overlayed on reconstruction. Trajectories for dorsal and ventral transects are also shown (white dotted lines). (*d*–*g*) FEM VM microstrain maps of the left coxa. White regions exceed scale (8×10^{-4} με). (*d*) Anterior view; black dotted line shows axis of rotation. (*e*) Posterior view. (*f*) Sagittal view, showing constrained gnathobases that are first involved in processing. (*g*) Close up of gnathobases (ar, axis of rotation; cg, constrained gnathobases; da, distal area; ki, coxal kink; pa, proximal area).

long axis of muscle fibres [45,46]. Segmented muscles were imported into Geomagic Studio and MCSA values were calculated using the 'Compute' tool. MCSA values were converted into maximum muscle force to inform the FEM using a conversion of 0.25 N mm^{-2} [47] (table S1 [70]). Coxa was solid-meshed in 3-matic v. 9.0 (Materialise, Leuven, Belgium). *Limulus polyphemus* coxa cuticle was modelled as a solid homogeneous structure. This will influence absolute stress/strain magnitudes, but results remain informative in purely comparative, shape-related contexts, as *Sidneyia inexpectans* was modelled similarly. The widely applied comparative FEA method that yields relative as opposed to absolute predictions was therefore used and the role of geometry in determining mechanical performance was explored [37,47–49]. The left *L. polyphemus* coxa model was imported as a Nastran (NAS) file into Strand7 (Strand7 Pty Ltd, Sydney, Australia) FEA software [50]. The model was treated as isotropic with Young's modulus of 867 N mm^{-2} (for sclerotized cuticle [51]) and a Poisson ratio of 0.3 (for isometric cuticle [35]). Muscle origins were tessellated as plate elements onto the meshed surface and modelled as 3D membrane (thickness = 0.0001 mm). Forces for each muscle, directed toward their respective insertion sites, were then applied to plate elements using Boneload [50,52]. Muscle insertions were treated as single points and identified using the 'point coordinates' tool in Geomagic Studio. The four largest, dorsally located gnathobases were constrained in all directions at the most apical node in Strand7 (figure 1*d*,*e*). These gnathobases were constrained to accurately reflect the mechanics of *L. polyphemus* appendages during mastication (as observed in the validation test; discussed below); constraining all gnathobases would have produced an unrealistic loading scenario. The coxa was constrained, but allowed to rotate about the coxal hinge. After FEM was solved, a colour-coded von Mises (VM) microstrain map was generated in Strand7 and reaction force magnitudes at the constrained nodes on the gnathobases were output from Strand7 in newtons.

The *L. polyphemus* validation test was conducted using a live female individual of similar size to the modelled specimen. This specimen, housed at the University of New Hampshire, was induced to process food using small (less than 1 cm) slices of lobster meat placed at the coxal bases. During processing, a FSR 402 force-sensitive resistor (Interlink Electronics, Westlake Village, CA) was placed between the posterior coxae and force measurements (in force-grams) recorded every 0.5 s. An Arduino-based data logging system, previously used to measure crab claw force (J. S. Goldstein 2017, personal communication), recorded the *L. polyphemus* bite force data. Force-gram measurements were converted into newtons to compare with FEM data. Shells were also fed to the individual to confirm it was capable of durophagy. Shells less than 1.5 cm long and less than 0.5 mm thick could be crushed by cephalothoracic appendages V and VI. We also noted that not all gnathobases are engaged in mastication at the same time: the most dorsally located spines perform initial processing.

(b) *Sidneyia inexpectans* model

A 3D reconstruction of the *S. inexpectans* thoracic appendage (exopod, endopod and protopodite) was made in Zbrush (Pixologic, Inc) (figure 2*c*–*e*). Micro-CT scanning of *S. inexpectans* was not possible as fossils are preserved as 2D carbon films on shale and the density difference between carbon and rock matrix is

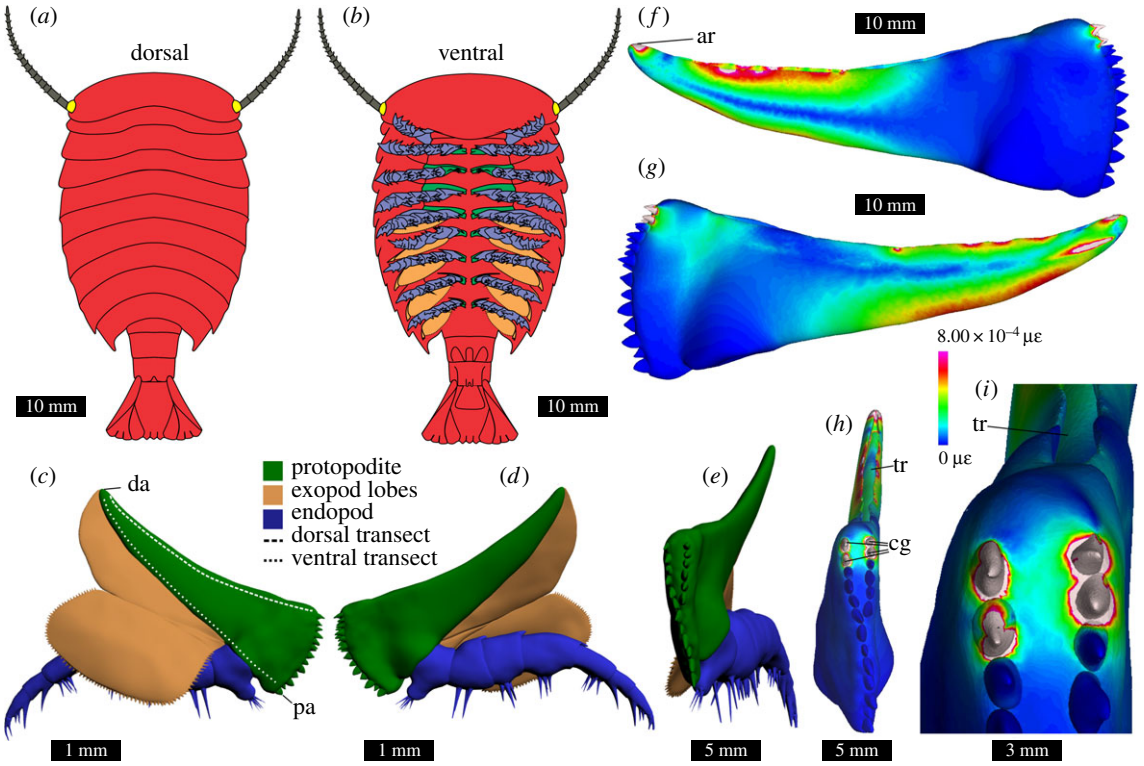

Figure 2. 2D and 3D reconstructions and VM microstrain maps of *Sidneyia inexpectans*. (*a*,*b*) Reconstruction of *S. inexpectans*, modified after Bruton [22]. (*a*) Dorsal view. (*b*) Ventral view; appendages are colour-coded to match 3D reconstructions (*c*–*e*). (*c*–*e*) Thoracic appendage showing only the major rami in various views, modified after Stein [24]. The 3D PDF is presented in figure S2 [70]. (*c*) Posterior view; trajectories for dorsal and ventral transects are shown (white dotted lines). (*d*) Anterior view. (*e*) Oblique view showing two rows of gnathobases. (*f*–*i*) FEM VM microstrain maps of the protopodite scaled to *Limulus polyphemus* volume. White regions exceed scale (8×10^{-4} με). (*f*) Posterior view. (*g*) Anterior view. (*h*) Sagittal view, showing the constrained gnathobases (chosen because of their relative positions on the *L. polyphemus* coxa). (*i*) Close up of the constrained gnathobases. Size scale of *S. inexpectans* reconstruction represents the actual size of fossil specimens. Size of *S. inexpectans* appendage (as indicated by scale bars in *c*–*i*) is scaled up to *L. polyphemus* model (ar, axis of rotation; cg, constrained gnathobases; da, distal area; pa, proximal area; tr, trough).

insufficient for scanning. Morphological details of the reconstruction (e.g. approximating relative dimensions of segments and spines) were based on published images of several thoracic appendage specimens of similar size, with some preserved at different orientations relative to the sediment laminations, allowing different perspectives to be considered [4,19,22,24]. As specimens are preserved in 2D, the third dimension—especially the 'inflation' of the protopodite—was extrapolated by comparing similar-sized *L. polyphemus* appendages, in addition to the relative dimensions of broadly comparable gnathobasic mandibles in modern copepod crustaceans [11]. Our reconstruction most closely resembles that illustrated by Stein ([24], fig. 9). However, two key differences are apparent, following recent observations by Bicknell *et al.* [4]. (1) The protopodite in our reconstruction has two rows of gnathobasic spines that 'v' into a single row towards the ventral section, as seen in both *L. polyphemus* and *Eurypterus tetragonophthalmus* [4,17,53]; Stein [24] reconstructed only one row of gnathobases. (2) Gnathobases in our reconstruction show a saw-toothed pattern with spines of alternating sizes, whereas Stein [24] showed a slight size gradation of spines along the gnathal edge. Thoracic appendage components were converted into .STL files in Zbrush and a 3D PDF was generated using 3D Reviewer. Distinct elements were assigned different colours and the 3D PDF is presented as a supplementary file (figure S2 [70]).

Boundary and loading conditions applied to *Sidneyia inexpectans* follow those applied to the *Limulus polyphemus* model to assess shape difference. First, the *S. inexpectans* model was scaled up to the same volume as the *L. polyphemus* coxa in Geomagic Studio [36,54,55]. Scaling up was conducted as *S. inexpectans* has a maximum exoskeletal length of 13 cm [22], which is much smaller than *L. polyphemus* (*ca* 24 cm without telson [56]); furthermore, extinct taxa should be scaled to the modern analogue (e.g. by scaling models to the same volume and loading parameters [55,57], or scaling muscle forces to the size of the fossil organism using a two-thirds power relationship [38]). A trough was constructed on the dorsal side of the protopodite for muscle origins (figure 2*h*,*i*). The muscle groups in *L. polyphemus* are assumed to be analogous to *S. inexpectans*, as muscles or scars are not preserved in the fossils. Size and locality (particularly origins and insertions) of muscles in *S. inexpectans* were estimated by comparing the morphology of the *L. polyphemus* coxa, particularly the trajectory and length of muscles 38, 39 and 40. The *L. polyphemus* muscle force magnitudes were used for *S. inexpectans*, as the models are of the same volume [52] (tables S1 and S2 [70]). Four dorsally located gnathobasic spines—considered to be functionally homologous to those in *L. polyphemus* (figure 1*g*), based on their relative positions and orientations on the coxa/protopodite of both taxa—were used to constrain the *S. inexpectans* model (figure 2*i*). This allowed a direct comparison with the *L. polyphemus* model. A colour-coded VM microstrain map was produced, but no reaction forces were calculated as the scaled model would have produced unrealistic reaction forces for a *S. inexpectans* individual that is considerably bigger than the largest known specimens of this species.

Brick elements were selected at equidistant points along the dorsal and ventral sides of the models (figures 1*c* and 2*c*) to assess changes in VM microstrain magnitudes and distributions between the two FE models. VM values at nodes were found by averaging microstrain of the six bricks around the nodes (following [58]). These values were analysed using a two-sample Anderson–Darling test. The non-parametric analysis assumes that a dataset is drawn from the same distribution as a second

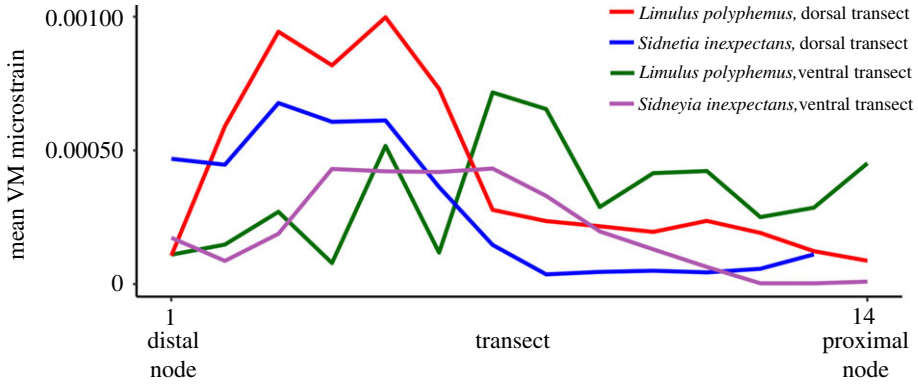

Figure 3. Distribution of mean VM microstrain values along dorsal and ventral transects of the two models. Most proximal node on the *Sidneyia inexpectans* dorsal transect was not included because the node was close to a constrained gnathobase.

dataset [59] and can therefore be applied to the non-normal data and small sample sizes collected here [60]. The analysis tests the following hypotheses:

> H_0: The two datasets are from the same distribution. Here, the two transects are statistically similar and therefore the two features are functionally similar: both taxa were durophagous predators/scavengers that operated in a similar way.
>
> H_1: The two datasets are from different distributions. Here, the two transects are statistically different and therefore the two features are functionally different: *S. inexpectans* used its similar morphology in a functionally different way to *L. polyphemus*.

VM microstrain values along the dorsal transects were analysed separate to the VM microstrain values from the ventral transects. The most distal point of the *L. polyphemus* transect was omitted as 13 points were collected for the *S. inexpectans* dorsal transect. Analyses were run using 1000 simulations in an R environment using the *kSamples* [61] package.

3. Results

The magnitudes and distributions of VM microstrain in the *L. polyphemus* model are similar to those generated in the *S. inexpectans* model (compare figures 1*d–g* with 2*f–i*). The *L. polyphemus* model displays high levels of VM microstrain along the dorsal portion of the coxa, with very high VM microstrain at the coxal kink, and generally lower VM microstrain along the ventral section (figure 1*d–f*). The anterior–posterior (A-P) VM microstrain distribution is asymmetrical, with slightly higher VM microstrain on the anterior side of the coxa (figure 1*d*,*e*). *Sidneyia inexpectans* experienced highest VM microstrain along the dorsal and ventral sides of the distal portion of the protopodite (figure 2*f*,*g*). No areas of extreme VM microstrain were noted, other than at the constraints, which contrasts with the *L. polyphemus* model. The A-P VM microstrain distribution for *S. inexpectans* is also asymmetrical (figure 2*f*,*g*).

Mean VM microstrain transects follow similar trends in both models, especially the dorsal transects, although there is considerable variation along the ventral transect for *L. polyphemus* (figure 3). For the distal sections of each transect, both models have higher VM microstrain along the dorsal transects and lower VM microstrain along the ventral transects. This reverses around the transect midpoints of both models, where the ventral transects have slightly higher VM microstrain than the dorsal transects in the proximal sections. The VM microstrain peaks at more dorso-distal sections of the two models and decreases proximally from the areas of rotation. The ventral transects show that VM microstrain is generally higher in the proximal section of the *L. polyphemus* model, compared to the *S. inexpectans* model (figure 3). Constrained gnathobases are not considered, as the very high VM microstrain at these points is probably artefactual. The Anderson–Darling tests show that pairs of transects are from the same distributions (dorsal: $n = 13$, $p = 0.207$; ventral: $n = 14$, $p = 0.055$). We therefore fail to reject the null hypothesis in favour of the alternative for both datasets. Estimated reaction forces of the *L. polyphemus* FEM and validation force values are of the same order of magnitude. Validation values range between 0 and 3.5 N (with most values between 0.5 and 1 N), and FEM reaction forces range between 2.2 and 4.5 N (figure 4).

4. Discussion

FEA modelling demonstrates that the *S. inexpectans* protopodite was functionally similar to the *L. polyphemus* coxa. This is supported by the Anderson–Darling tests, which confirmed that transect pairs are from the same distribution. One obvious difference shown in the *L. polyphemus* model is the very high VM microstrain at the coxal kink—a feature that is lacking in the *S. inexpectans* protopodite. In addition, strain is more evenly distributed along the dorsal and ventral sections of the *S. inexpectans* protopodite compared to the *L. polyphemus* coxa. This might be expected due to the straighter and smooth dorso-ventral margins of the *S. inexpectans* protopodite. These results confirm our original assumption that *S. inexpectans* was a durophage with gnathobasic appendages that had a similar functional capability to those of *L. polyphemus*. However, the more widely distributed regions of VM microstrain, coupled with thicker gnathobases [4], suggests that *S. inexpectans* may have been a more effective shell crusher than *L. polyphemus*. Thick sclerotized cuticle observed in *S. inexpectans* gnathobases may have permitted them to absorb more force during processing without affecting nerve endings within the spines [4].

Heavily sclerotized shell-crushing features probably arose in the Cambrian as a means of capitalizing on the abundance of benthic biomineralized prey. Calcitic trilobites, in particular, are one of the most abundant groups in the Burgess Shale community [62,63]. Shelly gut contents show that *S. inexpectans* primarily consumed juvenile trilobites, and to a lesser extent small agnostid arthropods, plus calcitic

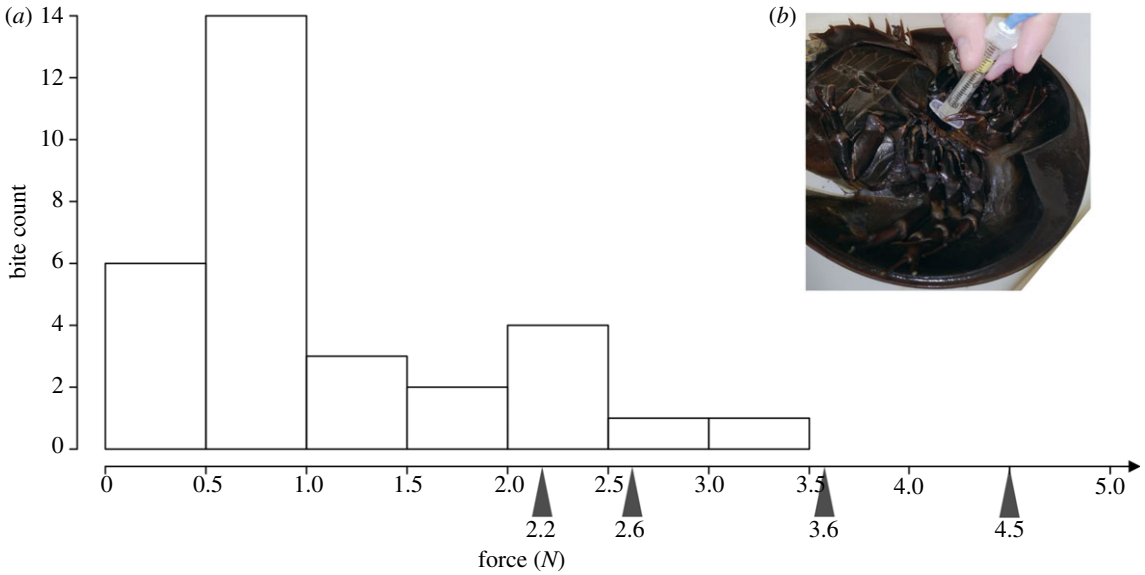

Figure 4. Distribution of bite force values from the *Limulus polyphemus* validation test, FEM reaction force values, and the device used to measure bite force. (*a*) Bite force and FEM reaction force data. The grey arrows are FEM values, each corresponding to a constrained gnathobase (figure 1*f*,*g*). (*b*) FSR 402 force-sensitive resistor (Interlink Electronics, Westlake Village, CA) placed between posterior coxae of the *L. polyphemus* specimen used for bite force test.

and phosphatic brachiopods [19]. This diet, and the lack of 'thick sclerotized or mineralized fragments' in the gut, suggests that *S. inexpectans* was perhaps limited to crushing only thin-shelled prey [19, p.215]. Yet, given the demonstrated biomechanical efficiency of the protopodite, its potential ability to crush thicker-shelled prey (such as adult trilobites) cannot be entirely dismissed. Notwithstanding, by exerting selective pressures on populations of juvenile trilobites and other small, thin-shelled prey, *S. inexpectans* potentially drove selection for more fortified shells or other novel defences in biomineralized prey within the Burgess Shale community over time [19,64]. However, despite strong evidence that *S. inexpectans* was a durophagous predator [19], scavenging as a commensurate or secondary feeding mode cannot be discounted, which would have downplayed its escalatory role in the phenotypic evolution of shelly prey.

Similarity of bite reaction forces to FEM reaction forces shows that FEMs of arthropods can produce results comparable to real-world values [32]. FEM values that are higher than the validation data reflect the upper limit of *L. polyphemus* bite force, demonstrating that even arthropods will not process with maximized force unless required [65]. The peak bite force value acquired from the validation test is lower than the maximum FEM reaction force values (figure 4). The food used to induce processing during the test explains this: lobster meat requires much less force than shells during mastication, resulting in lower forces than values predicted by the FEM. This is an important outcome, as FEMs can occasionally produce mixed results, with VM microstrain and stress magnitudes inconsistently reflecting reality [38,65–69]. One potential issue with the methodology is that MCSA values were used to inform the FEM. Muscle force values have errors ranging between 4.5 and 12.4%, and muscle staining may have shrunk muscle tissues [46]. However, agreement between the validation test and FEM reaction force data confirms that MCSA values obtained from iodine-stained specimens and micro-CT scans are reliable for arthropod FEA studies.

5. Conclusion

FE models of masticatory appendage structures of the Cambrian euarthropod *S. inexpectans* and its closest modern analogue *L. polyphemus* are presented. This premier comparative study demonstrates the mechanical performance of two durophagous arthropods with similar appendage morphology that are separated by more than 500 Myr. The FE microstrain map of the *L. polyphemus* coxa is comparable to the *S. inexpectans* protopodite, suggesting similar mechanical performance. However, the *S. inexpectans* model lacks concentrated areas of very high VM microstrain (compared to the coxal kink of *L. polyphemus*), suggesting that this Cambrian species may have been a more efficient durophage than the modern counterpart. When combined with other evidence, such as gnathobasic cuticle thickness and shelly gut contents, the FEA results convincingly demonstrate that *S. inexpectans* was an effective Cambrian shell-crushing arthropod. Furthermore, the effective use of heavily sclerotized masticatory structures would have impacted the benthic community of the Burgess Shale marine ecosystem, placing considerable selective pressures on shelly prey. Similarity of reaction force values from the *L. polyphemus* FEA to a bite force test on a live specimen validates the methodology developed here, demonstrating that FEA can be applied to studies on large modern arthropods. Our results show how useful 3D FEA is for not only understanding the biomechanics of modern arthropods, but also testing ideas regarding the functional morphology and lifestyles of extinct taxa.

Data accessibility. Virtual 3D PDFs of appendages can be viewed for free using Adobe Reader. The PDF and DAT files of the volume meshes used for FEA are also found at the Dryad Digital Repository: http://dx.doi.org/10.5061/dryad.d7s1183 [70].

Authors' contributions. R.D.C.B., J.R.P. and S.W. conceived the study. R.D.C.B., J.A.L., B.C.G. and W.H.W. collected and analysed the data. R.D.C.B., J.A.L. and S.W. interpreted the results, with input from the other authors. R.D.C.B., J.A.L. and J.R.P. wrote the text, and all authors discussed, edited and approved the manuscript.

Competing interests. We declare we have no competing interests.

Funding. This research is supported by funding from an Australian Postgraduate Award (to R.D.C.B.), a Keith and Dorothy Mackay Travelling Scholarship (to R.D.C.B.) and an Australian Research Council Future Fellowship (FT120100770 to J.R.P.).

Acknowledgements. Thanks to Katrina Kenny for producing the 3D reconstruction of the *S. inexpectans* appendage. We thank Mark Botton, Nicolás Campione, Jean-Bernard Caron, James Holmes, and Rudy Lerosey-Aubril for helpful information, discussions and feedback; Jason Goldstein for the use of the FSR 402 force-sensitive resistor; and associate editor John Hutchinson and the two anonymous referees for their helpful comments that led to a much improved manuscript.

References

1. Manton SM. 1964 Mandibular mechanisms and the evolution of arthropods. *Phil. Trans. R. Soc Lond. B* **247**, 1–183. (doi:10.1098/rstb.1964.0001)
2. Jago JB, García-Bellido DC, Gehling JG. 2016 An early Cambrian chelicerate from the Emu Bay Shale, South Australia. *Palaeontology* **59**, 549–562. (doi:10.1111/pala.12243)
3. Cong P, Daley AC, Edgecombe GD, Hou X. 2017 The functional head of the Cambrian radiodontan (stem-group Euarthropoda) *Amplectobelua symbrachiata*. *BMC Evol. Biol.* **17**, 208. (doi10.1186/s12862-017-1049-1)
4. Bicknell RDC, Paterson JR, Caron J-B, Skovsted CB. 2018 The gnathobasic spine microstructure of Recent and Silurian chelicerates and the Cambrian artiopodan *Sidneyia*: functional and evolutionary implications. *Arthropod. Struct. Dev.* **47**, 12–24. (doi:10.1016/j.asd.2017.12.001)
5. Yang J, Ortega-Hernández J, Legg DA, Lan T, Hou J-B, Zhang X-G. 2018 Early Cambrian fuxianhuiids from China reveal origin of the gnathobasic protopodite in euarthropods. *Nat. Commun.* **9**, 470. (doi:10.1038/s41467-017-02754-z)
6. Poschmann M, Schoenemann B, McCoy VE. 2016 Telltale eyes: the lateral visual systems of Rhenish Lower Devonian eurypterids (Arthropoda, Chelicerata) and their palaeobiological implications. *Palaeontology* **59**, 295–304. (doi:10.1111/pala.12228)
7. Shultz JW. 2001 Gross muscular anatomy of *Limulus polyphemus* (Xiphosura, Chelicerata) and its bearing on evolution in the Arachnida. *J. Arachnol.* **29**, 283–303. (doi:10.1636/0161-8202(2001)029[0283:gmaolp]2.0.co;2)
8. Zeng H, Zhao F, Yin Z, Zhu M. 2017 Appendages of an early Cambrian metadoxidid trilobite from Yunnan, SW China support mandibulate affinities of trilobites and artiopods. *Geol. Mag.* **154**, 1306–1328. (doi:10.1017/s0016756817000279)
9. Whittington HB. 1980 Exoskeleton, moult stage, appendage morphology, and habits of the Middle Cambrian trilobite *Olenoides serratus*. *Palaeontology* **23**, 171–204.
10. Michels J, Vogt J, Gorb SN. 2012 Tools for crushing diatoms—opal teeth in copepods feature a rubber-like bearing composed of resilin. *Sci. Rep.* **2**, 465. (doi:10.1038/srep00465)
11. Michels J, Schnack-Schiel SB. 2005 Feeding in dominant Antarctic copepods—does the morphology of the mandibular gnathobases relate to diet? *Mar. Biol.* **146**, 483–495. (doi:10.1007/s00227-004-1452-1)
12. Beccaloni J. 2009 *Arachnids*. Collingwood, Australia: CSIRO Publishing.
13. Botton ML. 1984 Diet and food preferences of the adult horseshoe crab *Limulus polyphemus* in Delaware Bay, New Jersey, USA. *Mar. Biol.* **81**, 199–207. (doi:10.1007/bf00393118)
14. Botton ML, Shuster CN, Keinath JA. 2003 Horseshoe crabs in a food web: who eats whom. In *The American horseshoe crab* (eds CN Shuster Jr, RB Barlow, HJ Brockmann), pp. 133–153. Cambridge, MA: Harvard University Press.
15. Bicknell RDC, Klinkhamer AJ, Flavel RJ, Wroe S, Paterson JR. 2018 A 3D anatomical atlas of appendage musculature in the chelicerate arthropod *Limulus polyphemus*. *PLoS ONE* **13**, e0191400. (doi:10.1371/journal.pone.0191400)
16. Wyse GA, Dwyer NK. 1973 The neuromuscular basis of coxal feeding and locomotory movements in *Limulus*. *Biol. Bull.* **144**, 567–579.
17. Selden PA. 1981 Functional morphology of the prosoma of *Baltoeurypterus tetragonophthalmus* (Fischer) (Chelicerata: Eurypterida). *Trans. R. Soc. Edinb. Earth Sci.* **72**, 9–48. (doi:10.1017/s0263593300003217)
18. Fortey RA, Owens RM. 1999 Feeding habits in trilobites. *Palaeontology* **42**, 429–465. (doi:10.1111/1475-4983.00080)
19. Zacaï A, Vannier J, Lerosey-Aubril R. 2016 Reconstructing the diet of a 505-million-year-old arthropod: *Sidneyia inexpectans* from the Burgess Shale fauna. *Arthropod. Struct. Dev.* **45**, 200–220. (doi:10.1016/j.asd.2015.09.003)
20. Bicknell RDC, Paterson JR. 2018 Reappraising the early evidence of durophagy and drilling predation in the fossil record: implications for escalation and the Cambrian Explosion. *Biol. Rev.* **93**, 754–784. (doi:10.1111/brv.12365)
21. Gould SJ. 1989 *Wonder life: the burgess shale and the nature of history*. New York, NY: WW Norton & Company.
22. Bruton DL. 1981 The arthropod *Sidneyia inexpectans*, Middle Cambrian, Burgess Shale, British Columbia. *Phil. Trans. R. Soc. Lond. B* **295**, 619–656. (doi:10.1098/rstb.1981.0164)
23. Bruton DL, Jensen A, Jacquet R. 1985 The use of models in the understanding of Cambrian arthropod morphology. *Trans. R. Soc. Edinb. Earth Sci.* **76**, 365–369. (doi:10.1017/S0263593300010579).
24. Stein M. 2013 Cephalic and appendage morphology of the Cambrian arthropod *Sidneyia inexpectans*. *Zoologischer Anzeiger* **253**, 164–178. (doi:10.1016/j.jcz.2013.05.001)
25. Cunningham JA, Rahman IA, Lautenschlager S, Rayfield EJ, Donoghue PCJ. 2014 A virtual world of paleontology. *Trends Ecol. Evol.* **29**, 347–357. (doi:0.1016/j.tree.2014.04.004)
26. Rayfield EJ. 2007 Finite element analysis and understanding the biomechanics and evolution of living and fossil organisms. *Annu. Rev. Earth Planet. Sci.* **35**, 541–576. (doi:10.1146/annurev.earth.35.031306.140104)
27. Kaliyamoorthy S, Zill SN, Quinn RD, Ritzmann RE, Choi J. 2001 Finite element analysis of strains in a *Blaberus* cockroach leg during climbing. *Intell. Robots Syst.* **2**, 833–838. (doi:10.1109/iros.2001.976272)
28. Combes SA, Daniel TL. 2003 Into thin air: contributions of aerodynamic and inertial-elastic forces to wing bending in the hawkmoth *Manduca sexta*. *J. Exp. Biol.* **206**, 2999–3006. (doi:10.1242/jeb.00502)
29. Herbert RC, Young PG, Smith CW, Wootton RJ, Evans KE. 2000 The hind wing of the desert locust (*Schistocerca gregaria* Forskal). III. A finite element analysis of a deployable structure. *J. Exp. Biol.* **203**, 2945–2955.
30. Ha NS, Truong QT, Goo NS, Park HC. 2013 Biomechanical properties of insect wings: the stress stiffening effects on the asymmetric bending of the *Allomyrina dichotoma* beetle's hind wing. *PLoS ONE* **8**, e80689. (doi:10.1371/journal.pone.0080689)
31. Schieber G *et al.* 2017 Hindwings of insects as concept generator for hingeless foldable shading systems. *Bioinspir. Biomim.* **13**, 016012. (doi:10.1088/1748-3190/aa979c)
32. Goyens J, Soons J, Aerts P, Dirckx J. 2014 Finite-element modelling reveals force modulation of jaw adductors in stag beetles. *J. R. Soc. Interface* **11**, 20140908. (doi:10.1098/rsif.2014.0908)
33. Blanke A, Watson PJ, Holbrey R, Fagan MJ. 2017 Computational biomechanics changes our view on insect head evolution. *Proc. R. Soc. B* **284**, 20162412. (doi:10.1098/rspb.2016.2412)
34. Hörnschemeyer T, Bond J, Young PG. 2013 Analysis of the functional morphology of mouthparts of the beetle *Priacma serrata*, and a discussion of possible food sources. *J. Insect Sci.* **13**, 1–14. (doi:10.1673/031.013.12601)
35. van der Meijden A, Kleinteich T, Coelho P. 2012 Packing a pinch: functional implications of chela shapes in scorpions using finite element analysis. *J. Anat.* **220**, 423–434. (doi:10.1111/j.1469-7580.2012.01485.x)
36. Blanke A, Schmitz H, Patera A, Dutel H, Fagan MJ. 2017 Form–function relationships in dragonfly mandibles under an evolutionary perspective.

J. R. Soc. Interface **14**, 20161038. (doi:10.1098/rsif.2016.1038)

37. Bright JA. 2014 A review of paleontological finite element models and their validity. *J. Paleontol.* **88**, 760–769. (doi:10.1666/13-090)
38. Attard MRG, Wilson LAB, Worthy TH, Scofield P, Johnston P, Parr WCH, Wroe S. 2016 Moa diet fits the bill: virtual reconstruction incorporating mummified remains and prediction of biomechanical performance in avian giants. *Proc. R. Soc. B* **283**, 20152043. (doi:10.1098/rspb.2015.2043)
39. McHenry CR, Wroe S, Clausen PD, Moreno K, Cunningham E. 2007 Supermodeled sabercat, predatory behavior in *Smilodon fatalis* revealed by high-resolution 3D computer simulation. *Proc. Natl Acad. Sci. USA* **104**, 16 010–16 015. (doi:10.1073/pnas.0706086104)
40. Ledogar JA *et al.* 2016 Mechanical evidence that *Australopithecus sediba* was limited in its ability to eat hard foods. *Nat. Commun.* **7**, 10596. (doi:10.1038/ncomms10596)
41. Metscher BD. 2009 MicroCT for comparative morphology: simple staining methods allow high-contrast 3D imaging of diverse non-mineralized animal tissues. *BMC Physiol.* **9**, 11. (doi:10.1186/1472-6793-9-11)
42. Gignac PM, Kley NJ. 2014 Iodine-enhanced micro-CT imaging: methodological refinements for the study of the soft-tissue anatomy of post-embryonic vertebrates. *J. Exp. Zool.* **322B**, 166–176. (doi:10.1002/jez.b.22561)
43. Lautenschlager S, Bright JA, Rayfield EJ. 2014 Digital dissection-using contrast-enhanced computed tomography scanning to elucidate hard- and soft-tissue anatomy in the Common Buzzard *Buteo buteo*. *J. Anat.* **224**, 412–431. (doi:10.1111/joa.12153)
44. Sharp AC, Trusler PW. 2015 Morphology of the jaw-closing musculature in the common wombat (*Vombatus ursinus*) using digital dissection and magnetic resonance imaging. *PLoS ONE* **10**, e0117730. (doi:10.1371/journal.pone.0117730)
45. Van Spronsen PH, Weijs WA, Valk J, Prahl-Andersen B, Van Ginkel FC. 1989 Comparison of jaw-muscle bite-force cross-sections obtained by means of magnetic resonance imaging and high-resolution CT scanning. *J. Dent. Res.* **68**, 1765–1770. (doi:10.1177/00220345890680120901)
46. Van Spronsen PH, Weijs WA, Valk J, Prahl-Andersen B, Van Ginkel FC. 1991 Relationships between jaw muscle cross-sections and craniofacial morphology in normal adults, studied with magnetic resonance imaging. *Eur. J. Orthod.* **13**, 351–361. (doi:10.1093/ejo/13.5.351)
47. Strait DS, Wang Q, Dechow PC, Ross CF, Richmond BG, Spencer MA, Patel BA. 2005 Modeling elastic properties in finite-element analysis: how much precision is needed to produce an accurate model? *Anatom. Rec.* **283**, 275–287. (doi:10.1002/ar.a.20172)
48. Fry BG *et al.* 2009 A central role for venom in predation by *Varanus komodoensis* (Komodo dragon) and the extinct giant *Varanus* (*Megalania*) *priscus*. *Proc. Natl Acad. Sci. USA* **106**, 8969–8974. (doi:10.1073/pnas.0810883106)
49. Wroe S *et al.* 2018 Computer simulations show that Neanderthal facial morphology represents adaptation to cold and high energy demands, but not heavy biting. *Proc. R. Soc. B* **285**, 20180085. (doi:10.1098/rspb.2018.0085)
50. Ledogar JA, Luk THY, Perry JMG, Neaux D, Wroe S. 2018 Biting mechanics and niche separation in a specialized clade of primate seed predators. *PLoS ONE* **13**, e0190689. (doi:10.1371/journal.pone.0190689)
51. Dalingwater JE. 1985 Biomechanical approaches to eurypterid cuticles and chelicerate exoskeletons. *Trans. R. Soc. Edinb Earth Sci.* **76**, 359–364. (doi:10.1017/s0263593300010567)
52. Grosse IR, Dumont ER, Coletta C, Tolleson A. 2007 Techniques for modeling muscle-induced forces in finite element models of skeletal structures. *Anatom. Rec.* **290**, 1069–1088. (doi:10.1002/ar.20568)
53. Eisenack A. 1956 Beobachtungen an Fragmenten von Eurypteriden-Panzern. *Neus Jahrbuch für Geologie und Palaontologie* **104**, 119–128.
54. Strait DS *et al.* 2010 The structural rigidity of the cranium of *Australopithecus africanus*: implications for diet, dietary adaptations, and the allometry of feeding biomechanics. *Anatom. Rec.* **293**, 583–593. (doi:10.1002/ar.21122)
55. Dumont ER, Grosse IR, Slater GJ. 2009 Requirements for comparing the performance of finite element models of biological structures. *J. Theor. Biol.* **256**, 96–103. (doi:10.1016/j.jtbi.2008.08.017)
56. Sekiguchi K, Seshimo H, Sugita H. 1988 Post-embryonic development of the horseshoe crab. *Biol. Bull.* **174**, 337–345.
57. D'Anastasio R *et al.* 2013 Micro-biomechanics of the Kebara 2 hyoid and its implications for speech in Neanderthals. *PLoS ONE* **8**, e82261. (doi:10.1371/journal.pone.0082261)
58. Attard MRG, Chamoli U, Ferrara TL, Rogers TL, Wroe S. 2011 Skull mechanics and implications for feeding behaviour in a large marsupial carnivore guild: the thylacine, Tasmanian devil and spotted-tailed quoll. *J. Zool.* **285**, 292–300. (doi:10.1111/j.1469-7998.2011.00844.x)
59. Engmann S, Cousineau D. 2011 Comparing distributions: the two-sample Anderson–Darling test as an alternative to the Kolmogorov–Smirnoff test. *J. Appl. Quant. Methods* **6**, 1–17.
60. Scholz FW, Stephens MA. 1987 K-sample Anderson–Darling tests. *J. Amer. Stat. Assoc.* **82**, 918–924. (doi:10.1080/01621459.1987.10478517)
61. Scholz FW, Zhu A. 2018 kSamples: k-sample rank tests and their combinations. See https://CRAN.R-project.org/package=kSamples.
62. Caron J.-B., Jackson D.A. 2006 Taphonomy of the Greater Phyllopod Bed community, Burgess Shale. *Palaios* **21**, 451–465. (doi:10.2110/palo.2003.P05-070R).
63. Caron J.-B., Jackson D.A. 2008 Paleoecology of the Greater Phyllopod Bed community, Burgess Shale. *Palaeogeogr. Palaeoclimatol. Palaeoecol.* **258**, 222–256. (doi10.1016/j.palaeo.2007.05.023)
64. Topper T.P., Strotz L.C., Holmer L.E., Zhang Z., Tait N.N., Caron J.-B. 2015 Competition and mimicry: the curious case of chaetae in brachiopods from the middle Cambrian Burgess Shale. *BMC Evol. Biol.* **15**, 42. (doi10.1186/s12862-015-0314-4)
65. Wroe S, McHenry C, Thomason J. 2005 Bite club: comparative bite force in big biting mammals and the prediction of predatory behaviour in fossil taxa. *Proc. R. Soc. B* **272**, 619–625. (doi:10.1098/rspb.2004.2986)
66. Metzger KA, Daniel WJT, Ross CF. 2005 Comparison of beam theory and finite-element analysis with *in vivo* bone strain data from the alligator cranium. *Anatom. Rec.* **283**, 331–348. (doi:10.1002/ar.a.20167)
67. Ledogar JA *et al.* 2016 Human feeding biomechanics: performance, variation, and functional constraints. *PeerJ* **4**, e2242. (doi:10.7287/peerj.preprints.2113v1)
68. Bright JA, Rayfield EJ. 2011 Sensitivity and *ex vivo* validation of finite element models of the domestic pig cranium. *J. Anat.* **219**, 456–471. (doi:10.1111/j.1469-7580.2011.01408.x)
69. Cuff AR, Bright JA, Rayfield EJ. 2015 Validation experiments on finite element models of an ostrich (*Struthio camelus*) cranium. *PeerJ* **3**, e1294. (doi:10.7717/peerj.1294)
70. Bicknell RDC, Ledogar JA, Wroe S, Gutzler BC, Watson III WH, Paterson JR. 2018 Data from: Computational biomechanical analyses demonstrate similar shell-crushing abilities in modern and ancient arthropods. Dryad Digital Repository. (doi:10.5061/dryad.d7s1183)